Extreme case of density scaling: The Weeks-Chandler-Andersen system at low temperatures

Eman Attia [*], Jeppe C. Dyre [†], and Ulf R. Pedersen [‡]
Glass and Time, IMFUFA, Department of Science and Environment, Roskilde University,
P.O. Box 260, 4000 Roskilde, Denmark

This paper studies numerically the Weeks-Chandler-Andersen system, which is shown to obey hidden scale invariance with a density-scaling exponent that varies from below 5 to above 500. This unprecedented variation makes it advantageous to use the fourth-order Runge-Kutta algorithm for tracing out isomorphs. Good isomorph invariance of structure and dynamics is observed over more than three orders of magnitude temperature variation. For all state points studied, the virial potential-energy correlation coefficient and the density-scaling exponent are controlled mainly by the temperature. Based on the assumption of statistically independent pair interactions, a mean-field theory is developed that rationalizes this finding and provides an excellent fit to data at low temperatures.

I. INTRODUCTION

Density scaling is an important experimental discovery of the past 20 years' liquid-state research, which by now has been demonstrated for high-pressure data of hundreds of systems [1–4]. The crucial insight is that, in order to characterize a thermodynamic state point, the relevant variable supplementing the temperature T is not the pressure p, but the number density $\rho \equiv N/V$ (considering N particles in volume V) [1–6]. If γ is the so-called density-scaling exponent, plotting data for the dynamics as a function of ρ^γ/T results in a collapse [1–4]. In other words, the dynamics depends on the two variables of the thermodynamic phase diagram only via the single variable ρ^γ/T. This provides a significant rationalization of data, as well as an important hint for theory development. It should be noted, though, that density scaling does not apply universally; for instance, it usually works better for van der Waals liquids than for hydrogen-bonded liquids [2,4].

Some time after these developments were initiated, a framework for density scaling was provided in terms of the isomorph theory [7,8], which links density scaling to Rosenfeld's excess-entropy scaling method [9,10]. According to isomorph theory, any system with strong correlations between the fixed-volume virial and potential-energy equilibrium fluctuations has curves of invariant structure and dynamics in the thermodynamic phase diagram. These "isomorphs" [7,11] are defined as curves of constant excess entropy S_{ex}, which is the entropy minus that of an ideal gas at the same temperature and density ($S_{ex} < 0$ because any system is more ordered than an ideal gas).

* attia@ruc.dk
† dyre@ruc.dk
‡ urp@ruc.dk

If the potential energy is denoted by U and the virial by W, their Pearson correlation coefficient R is defined by

$$R = \frac{\langle \Delta U \, \Delta W \rangle}{\sqrt{\langle (\Delta U)^2 \rangle \langle (\Delta W)^2 \rangle}}. \quad (1)$$

Here Δ denotes the deviation from the thermal average and the angular brackets are canonical (NVT) averages. The pragmatic criterion defining strong correlation is $R > 0.9$ [12,13]. Systems with strong correlations have good isomorphs, i.e., approximate invariance of structure and dynamics along the configurational adiabats [7]. Such systems are termed R-simple, signaling the simplification of having an effectively one-dimensional thermodynamic phase diagram in regard to structure and dynamics when these are given in so-called reduced units (discussed below). Hydrogen-bonded systems usually have $R < 0.9$ and are thus not R-simple [12]; this explains why density scaling does not apply universally.

Isomorph theory is only rigorously correct in the unrealistic case of an Euler-homogeneous potential-energy function that is realized, for instance, in systems with inverse-power-law (IPL) pair potentials [14]. Nevertheless, isomorph-theory predictions apply to a good approximation for many systems, e.g., Lennard-Jones-type liquids [7,15–17], the exponential pair-potential system at low temperatures [18,19], simple molecular models [20–22], polydisperse systems [23], crystals [24], nanoconfined liquids [25], polymerlike flexible molecules [26], metals [27,28], and Yukawa plasmas [29,30].

In some cases, isomorphs are well described by the equation $\rho^\gamma/T = \text{const}$ with a constant γ [31], which as mentioned accounts for density scaling as discussed in most experimental contexts [2]. Isomorph theory, however, does not require γ to be constant throughout the thermodynamic phase diagram, and γ indeed does vary in most simulations [16,32–34]. The general isomorph-theory definition of the density-scaling exponent γ at a given state point [7,10] is

$$\gamma \equiv \left(\frac{\partial \ln T}{\partial \ln \rho} \right)_{S_{ex}} = \frac{\langle \Delta U \, \Delta W \rangle}{\langle (\Delta U)^2 \rangle}. \quad (2)$$

The second equality gives the statistical-mechanical expression of γ in terms of the constant-volume canonical-ensemble fluctuations of potential energy and virial.

The question whether experimental density-scaling exponents are strictly constant throughout the phase diagram has recently come into focus [35,36]. In simulations, isomorphs are in many cases described by the equation [1,8,32,37]

$$\frac{h(\rho)}{T} = \text{const},\tag{3}$$

in which $h(\rho)$ is a function of the density. For the Lennard-Jones (LJ) system, for instance, one has $h(\rho) \propto (\gamma_0/2 - 1)(\rho/\rho_0)^4 - (\gamma_0/2 - 2)(\rho/\rho_0)^2$, in which γ_0 is the density-scaling exponent at a reference state point of density ρ_0 [32,37]. For isomorphs given by Eq. (3), Eq. (2) implies

$$\gamma = \frac{d \ln h(\rho)}{d \ln \rho}.\tag{4}$$

We see that unless $h(\rho)$ is a power-law function, the density-scaling exponent depends on the density. More generally, γ also depends on the temperature [33]. This is the case, for instance, for the LJ system approaching very high temperatures: For $T \to \infty$ at a fixed density, the LJ system is dominated by the repulsive r^{-12} term of the pair potential, implying that γ approaches $\frac{12}{3} = 4$ in this limit and that Eq. (3) cannot apply.

A likely reason that many experiments are well described by a constant γ is the fact that density often does not vary much. As shown by Casalini and co-workers [36,38], when extreme pressure is applied, the density-scaling exponent is no longer constant. Although it is now clear that γ is not a material constant [35,36], its variation is as mentioned often insignificant in experiments. This paper gives an example in which γ varies dramatically. We present a study of the noted Weeks-Chandler-Andersen (WCA) system [39,40] that 50 years ago introduced the idea of a cutoff at the potential-energy minimum of the LJ system [41–46]. This idea is still very popular and used in many different contexts [47–53].

We show below that the WCA system has strong virial potential-energy correlations and thus is R-simple. We find that γ varies by more than two decades in the investigated part of the phase diagram. In comparison, the LJ system has a density-scaling exponent that varies less than 50% throughout the phase diagram. To the best of our knowledge, the γ variation of the WCA system is much larger than has so far been reported for any system in simulations or experiments. For all state points studied, we find that γ depends primarily on the temperature. A mean-field theory is presented that explains this observation and accounts well for the low-temperature and low-density behavior of the system.

After providing a few technical details in Sec. II, we present the thermodynamic phase diagram with the state points studied numerically in Sec. III. The paper's focus is on three isomorphs, numbered 1–3. Each of these is associated with an isotherm and an isochore, the purpose of which is to put into perspective the isomorph variation of structure and dynamics by comparing it to what happens when a similar density or temperature variation is studied, keeping the other variable constant. In Sec. III we also give data for the virial potential-energy correlation coefficient R and the

density-scaling exponent γ, demonstrating that all state points studied have strong correlations ($R > 0.9$) while γ varies from about 5 to above 500. A mean-field theory is developed in Sec. IV, predicting that R and γ both depend primarily on the temperature. Section V presents simulations of the structure and dynamics along the isotherms, isochores, and isomorphs. Despite the extreme γ variation, which implies that an approximate inverse-power-law description fails entirely, we find good isomorph invariance of the reduced-unit structure and excellent isomorph invariance of the reduced-unit dynamics. Section VI gives a brief discussion. The Appendix details the implementation of the fourth-order Runge-Kutta method for tracing out isomorphs and compares its predictions to those of the previously used simple Euler method.

II. MODEL AND SIMULATION DETAILS

Liquid model systems are often defined in terms of a pair potential $v(r)$. If $r_{ij} = |\mathbf{r}_i - \mathbf{r}_j|$ is the distance between particles i and j, the potential energy U as a function of all particle coordinates $\mathbf{R} \equiv (\mathbf{r}_1, \mathbf{r}_2, \ldots, \mathbf{r}_N)$ is given by

$$U(\mathbf{R}) = \sum_{i<j} v(\mathbf{r}_{ij}).\tag{5}$$

We study in this paper the single-component WCA system [39], which cuts the standard LJ pair potential at its minimum and subsequently shifts the potential by adding a constant such that the minimum is lifted to zero [39,54]. The result is the purely repulsive pair potential given by

$$v(r) = \begin{cases} 4\varepsilon\left[\left(\frac{r}{\sigma}\right)^{-12} - \left(\frac{r}{\sigma}\right)^{-6}\right] + \varepsilon & (r < 2^{1/6}\sigma) \\ 0 & (r > 2^{1/6}\sigma). \end{cases}\tag{6}$$

Like the LJ pair potential, $v(r)$ involves two parameters: σ that reflects the particle radius and ε that is the numerical value of the energy of the LJ potential at its minimum at $r = 2^{1/6}\sigma$.

The WCA system was studied by molecular dynamics (MD) simulations in the canonical (NVT) ensemble using the Nosé-Hoover thermostat [55]. The simulated system consisted of 4000 particles in a cubic box with periodic boundaries. The simulations were performed using the open-source Roskilde University molecular dynamics software (RUMD) that runs on GPUs (graphics processing units) [56,57]. For updating the system state, the leapfrog algorithm was employed with a reduced-unit time step of 0.0025. At each state point, a simulation first ran for 25×10^6 time steps for equilibration. This was followed by 50×10^6 time steps for the production run.

The simulations were conducted in the reduced-unit system of isomorph theory in which the energy unit is $e_0 \equiv k_B T$, the length unit is $l_0 \equiv \rho^{-1/3}$, and the time unit is $t_0 \equiv \rho^{-1/3}\sqrt{m/k_B T}$, where m is the particle mass [7]. A few simulations were also carried out in MD units to check for consistency. Using reduced units in a simulation implies that density and temperature are both equal to unity; the state point is changed by varying σ and ε, i.e., by changing the pair potential. In contrast, performing simulations in MD units implies setting $\sigma = \varepsilon = 1$, i.e., fixing the pair potential and varying ρ and T in order to change the state point. The two methods are mathematically equivalent, of course. Simulating
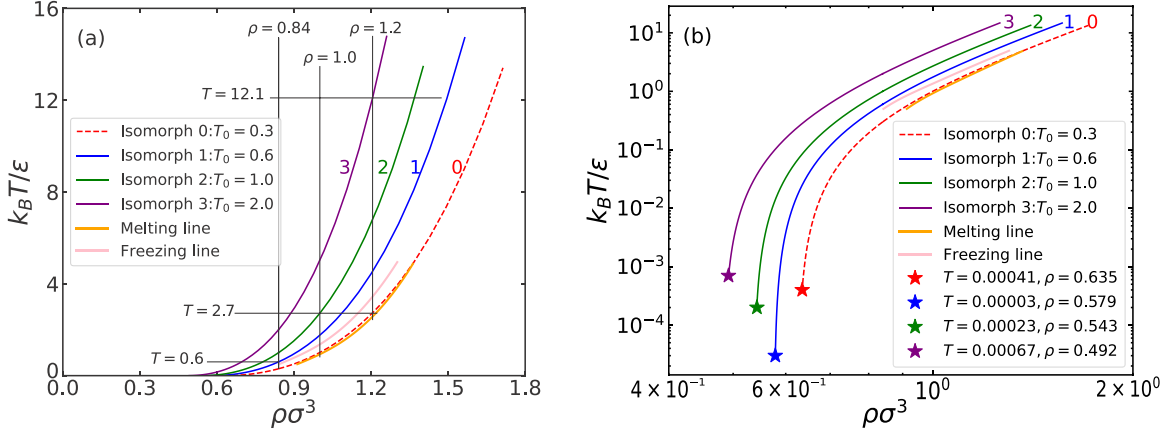
FIG. 1. (a) The three isomorphs in focus (denoted by 1–3) shown as full curves in the temperature-density thermodynamic phase diagram. Each isomorph was generated as described in the text and in the Appendix, starting from the reference state point (ρ_0, T_0) with $\rho_0 = 0.84$ and T_0 equal to 0.6, 1.0, and 2.0, respectively. A fourth isomorph (denoted by 0) marked by the red dashed line is in the supercooled liquid phase. The horizontal lines are three isotherms and the vertical lines are three isochores, which are studied in order to compare their structure and dynamics variation to those along the isomorphs. The freezing and melting lines are shown as yellow and orange lines, respectively [41,45]; note that these are parallel to the isomorphs. (b) The four isomorphs shown in a logarithmic temperature-density phase diagram. The slope γ [Eq. (2)] increases significantly as the temperature is lowered along an isomorph. The stars mark the lowest simulated temperature and density on each isomorph; these state points are used in Fig. 9 below.

in reduced units is convenient because the time step is then automatically adjusted to take into account the thermal velocity.

Reduced quantities are generally marked by a tilde, for instance, $\tilde{r} \equiv r/l_0 = \rho^{1/3} r$. These units are used below for all quantities except for the density and the temperature; thermodynamic state points are reported by giving density and temperature in standard MD units, i.e., ρ is given in units of σ^{-3} and T in units of ε/k_B.

III. SIMULATED STATE POINTS

Figure 1(a) shows the thermodynamic phase diagram of the WCA system. The yellow and orange lines are the freezing and melting lines [41,45]. The blue, green, and purple lines marked 1, 2, and 3, respectively, are the isomorphs of main focus below, while the red dashed line is a fourth isomorph marked 0, which is in the liquid-solid coexistence region. Note that the freezing and melting lines are both approximate isomorphs [7,58].

Each isomorph was traced out starting from a reference state point of density 0.84. Isomorphs are often identified by integrating Eq. (2) using the simple first-order Euler integration scheme for density changes of order 1% [7,16,20]. The extreme variation of γ found for the WCA system, however, means that Euler integration can only be used reliably for very small density changes and a more accurate integration scheme is called for. We used the fourth-order Runge-Kutta integration (RK4) as detailed in the Appendix, where it is demonstrated that RK4 is 10–100 times more computationally efficient than Euler integration for tracing out isomorphs with a given accuracy. Data for selected state points of the four isomorphs are listed in Table I.

In order to investigate the degree of isomorph invariance of the reduced-unit structure and dynamics (Sec. V), for each isomorph we also performed simulations along an isotherm and an isochore, limiting all simulations to state points in the

equilibrium liquid phase. Figure 1(b) shows the isomorphs and the melting and freezing lines in a diagram with logarithmic density and temperature axes. In this diagram the density-scaling exponent γ is the isomorph slopes [compare Eq. (2)], which increases significantly along each isomorph as the density is lowered.

A configurational adiabat is an isomorph only for state points with strong virial potential-energy correlations, i.e., when $R \gtrsim 0.9$ at the relevant state points in which R is given by Eq. (1). This condition is validated in Fig. 2, which shows R for all state points simulated. Figure 2(a) shows R as a function of the density, while Fig. 2(b) shows R as a function of the temperature. We see that R increases with increasing density and temperature, approaching unity. This reflects the fact that the $(r/\sigma)^{-12}$ term of the pair potential dominates the interactions in these limits and that an IPL pair potential has $R = 1$. An important observation from Fig. 2 is that strong correlations are maintained even at the lowest densities and temperatures studied. A comparison of Figs. 2(a) and 2(b) reveals that R is primarily controlled by the temperature. This may be understood from a mean-field theory, which assumes that the interactions at low temperatures and densities are dominated by single-pair interactions (Sec. IV).

Figure 3 gives data for the density-scaling exponent γ at the state points simulated, plotted in different ways using the same symbols as in Fig. 2. We see that γ increases monotonically as either density, pressure, or temperature is lowered, eventually reaching values above 500. Figure 3(a) shows γ as a function of the density ρ. Clearly, knowledge of ρ is not enough to determine γ, implying that Eq. (4) does not apply for the WCA system. It has been suggested that γ is controlled by the pressure [59]. This works better than the density for collapsing data, but there is still some scatter [Fig. 3(b)]. Figure 3(c) plots γ as a function of the temperature. We here observe a quite good collapse, concluding that

TABLE I. State-point data for (a) isomorph 0, (b) isomorph 1, (c) isomorph 2, and (d) isomorph 3 (see Fig. 1).

$\rho\sigma^3$	k_BT/ε	$P\sigma^3/\varepsilon$	γ	R	$U/N\varepsilon$	$W/N\varepsilon$
			(a)			
1.714	13.41	464.2	4.288	0.9995	50.67	257.5
1.636	10.98	357.7	4.329	0.9993	39.92	207.7
1.493	7.360	211.9	4.435	0.9988	24.52	134.6
1.366	4.933	125.2	4.582	0.9978	14.84	86.70
1.254	3.307	73.86	4.787	0.9961	8.841	55.59
1.156	2.217	43.60	5.068	0.9936	5.190	35.49
1.071	1.486	25.81	5.445	0.9902	3.007	22.60
0.9985	0.9960	15.35	5.939	0.9860	1.721	14.38
0.9364	0.6677	9.200	6.571	0.9808	1.298	9.157
0.9091	0.5466	7.145	6.945	0.9782	0.7332	7.313
0.8610	0.3664	4.341	7.835	0.9726	0.4117	4.675
0.8400	0.3000	3.396	8.353	0.9698	0.3079	3.743
0.8207	0.2456	2.664	8.932	0.9671	0.2300	2.100
0.7592	0.1104	1.034	11.94	0.9566	0.0711	1.251
0.7168	0.04960	0.4159	16.42	0.9475	0.0218	0.5306
0.6877	0.02230	0.1725	23.09	0.9402	0.006653	0.2285
0.6680	0.009059	0.06587	33.06	0.9349	0.001742	0.08984
0.6546	0.004972	0.03509	47.83	0.9304	0.0007115	0.04379
0.6456	0.002021	0.01382	69.90	0.9277	0.0001853	0.01938
0.6353	0.0004081	0.002703	152.0	0.9243	0.00001690	0.003846
			(b)			
1.565	14.72	340.4	4.337	0.9993	39.48	202.9
1.495	12.05	262.7	4.385	0.9991	31.11	163.7
1.366	8.078	156.1	4.506	0.9983	19.14	106.2
1.252	5.415	92.69	4.671	0.9971	11.61	68.63
1.151	3.630	55.03	4.893	0.9954	6.956	44.18
1.024	1.992	25.27	5.366	0.9913	3.149	22.70
0.9527	1.335	15.12	5.799	0.9875	1.830	14.53
0.8916	0.8951	9.101	6.351	0.9831	1.053	9.310
0.8400	0.6000	5.520	7.041	0.9782	0.6015	5.972
0.7961	0.4022	3.377	7.899	0.9730	0.3412	3.840
0.7590	0.2696	2.085	8.955	0.9677	0.1925	2.477
0.7280	0.1807	1.299	10.25	0.9624	0.1081	1.603
0.7019	0.1211	0.8161	11.84	0.9574	0.06048	1.041
0.6708	0.06648	0.4129	14.88	0.9504	0.02517	0.5491
0.6543	0.04456	0.2646	17.48	0.9465	0.01399	0.3598
0.6245	0.01639	0.08940	26.75	0.9380	0.003198	0.1268
0.6060	0.006031	0.03111	42.01	0.9319	0.0007245	0.04532
0.5945	0.002219	0.01105	67.19	0.9282	0.0001632	0.01637
0.5787	0.00002724	0.0001290	579.6	0.9222	0.0000002251	0.0001957
			(c)			
1.403	13.46	219.9	4.415	0.9989	27.20	143.3
1.341	11.02	169.8	4.474	0.9985	21.39	115.6
1.228	7.389	101.2	4.620	0.9976	13.12	75.04
1.128	4.953	60.34	4.814	0.9961	7.946	48.53
1.040	3.320	36.01	5.070	0.9940	4.756	31.30
1.001	2.718	27.85	5.225	0.9926	3.664	25.11
0.9637	2.226	21.56	5.399	0.9919	2.814	20.14
0.8972	1.492	12.96	5.820	0.9876	1.648	12.95
0.8675	1.221	10.07	6.071	0.9856	1.256	10.39
0.8400	1.000	7.837	6.350	0.9834	0.9557	8.330
0.8146	0.8187	6.110	6.663	0.9811	0.7256	6.683
0.7494	0.4493	2.930	7.828	0.9737	0.3141	3.461
0.6987	0.2466	1.432	9.411	0.9659	0.1342	1.803
0.6295	0.07427	0.3613	14.45	0.9515	0.02378	0.4998
0.5945	0.02734	0.1204	21.64	0.9420	0.005505	0.1752

TABLE I. (*Continued.*)

$\rho\sigma^3$	k_BT/ε	$P\sigma^3/\varepsilon$	γ	R	$U/N\varepsilon$	$W/N\varepsilon$
0.5694	0.008230	0.03360	36.68	0.9337	0.0009355	0.05084
0.5591	0.003698	0.01464	53.01	0.9300	0.0002851	0.02248
0.5507	0.001360	0.005242	85.02	0.9268	0.00006423	0.008158
0.5436	0.0002747	0.001034	185.1	0.9238	0.000005878	0.001628
			(d)			
1.261	14.79	160.7	4.468	0.9986	21.25	112.7
1.206	12.10	124.4	4.531	0.9982	91.04	16.73
1.106	8.110	74.47	4.687	0.9971	10.30	59.25
1.060	6.640	57.64	4.781	0.996	8.044	47.75
0.9766	4.451	34.57	5.011	0.9946	4.870	30.95
0.9389	3.644	26.80	5.148	0.9934	3.774	24.90
0.9036	2.984	20.79	5.304	0.9922	2.917	20.03
0.8400	2.000	12.55	5.675	0.9890	1.730	12.94
0.8114	1.638	9.771	5.892	0.9873	1.327	10.41
0.7603	1.098	5.947	6.410	0.9833	0.7760	6.725
0.6787	0.4932	2.248	7.836	0.9741	0.2592	2.820
0.6196	0.2216	0.8762	9.977	0.9641	0.08440	1.192
0.5776	0.0996	0.3520	13.15	0.9548	0.02690	0.5098
0.5481	0.04474	0.1453	17.89	0.9466	0.008466	0.2204
0.5276	0.02010	0.06135	24.92	0.9395	0.002630	0.09617
0.5135	0.009033	0.02636	35.42	0.9347	0.0008093	0.04231
0.5038	0.004059	0.01148	50.9571	0.9305	0.0002475	0.01873
0.4973	0.001824	0.005048	74.1566	0.9278	0.00007535	0.008328
0.4920	0.0006709	0.001824	119.9858	0.9254	0.00001656	0.003037

γ is primarily controlled by the temperature. Figures 3(d)–3(f) show data for all the state points simulated in logarithmic plots as functions of density, pressure, and temperature, respectively.

IV. MEAN-FIELD THEORY FOR R AND γ AT LOW DENSITIES

This section presents a mean-field theory for estimating the virial potential-energy correlation coefficient R and the density-scaling exponent γ. Along the lines of Refs. [18,33,60,61], we assume that the individual pair interactions are statistically independent; this is expected to be a good approximation at relatively low densities.

In MD units the truncated WCA pair potential (6) is

$$v(r) = 4r^{-12} - 4r^{-6} + 1 \quad \text{for } r < r_c \equiv 2^{1/6} = 1.122\ldots \tag{7}$$

and zero otherwise. The virial of the configuration $\mathbf{R}$ is given by $W(\mathbf{R}) = \sum_{i>j}^{N} w(r_{ij})$, in which the pair virial is defined as $w(r) \equiv -(r/3)v'(r)$ [55]. Although the WCA potential is
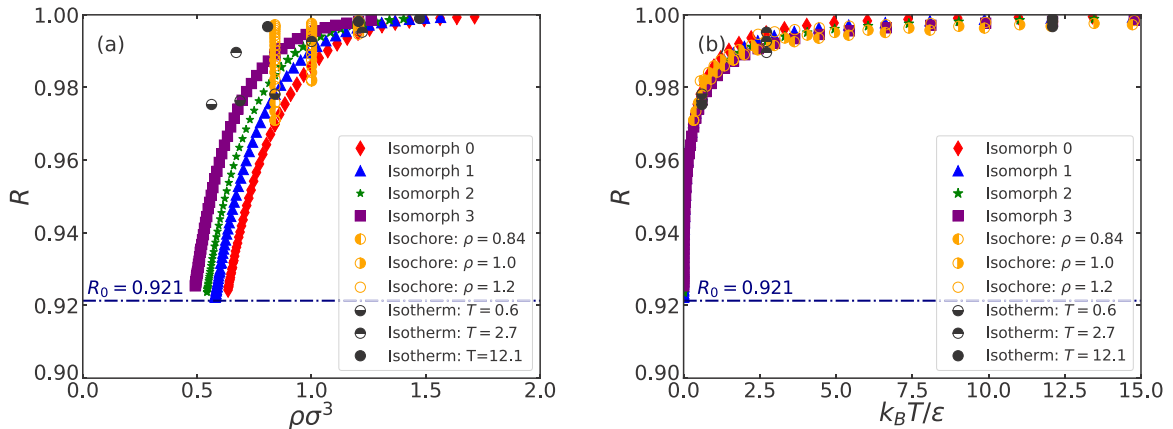

FIG. 2. Virial potential-energy correlation coefficient R [Eq. (1)] for all state points studied (Fig. 1): (a) R as a function of the density, (b) R as a function of the temperature. There are strong correlations everywhere ($R > 0.9$). The horizontal dash-dotted lines mark the low-temperature low-density limit of the mean-field-theory prediction $R_0 = \sqrt{8/3\pi} = 0.921$ [Eq. (20)]. The correlations are mainly controlled by the temperature.
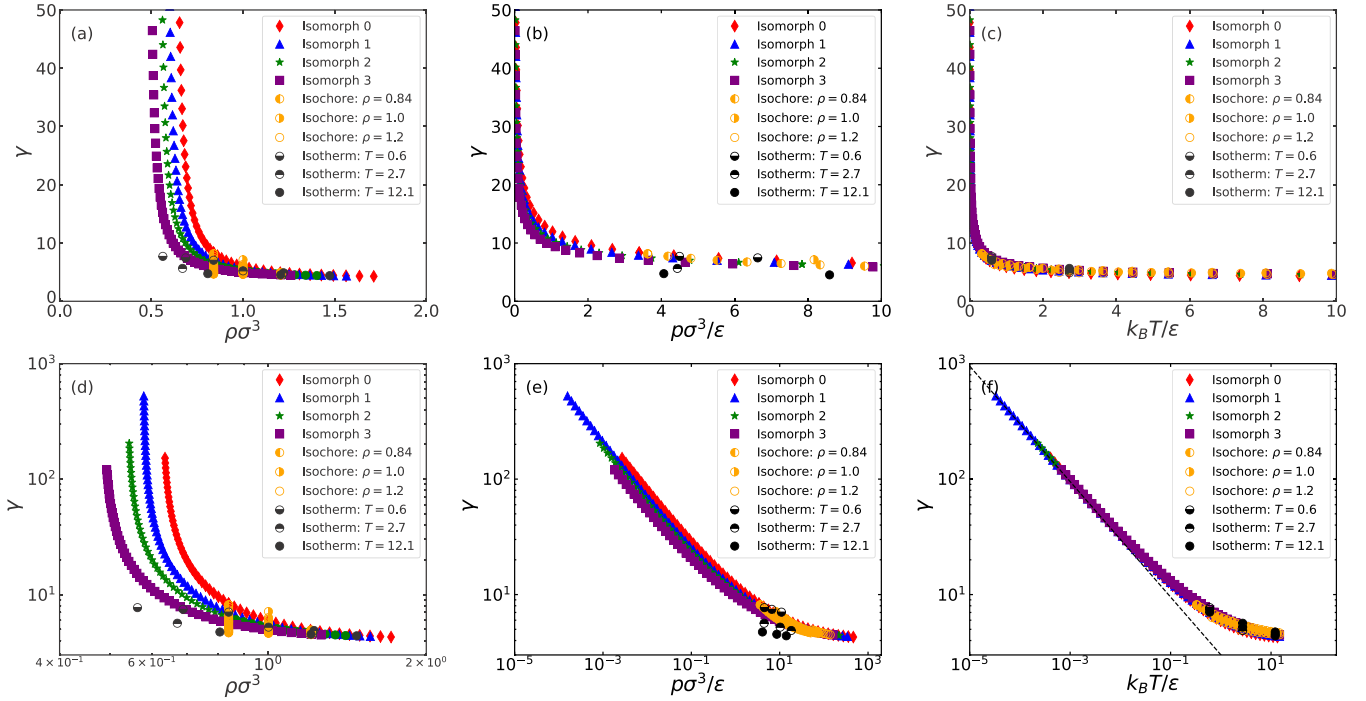
FIG. 3. Density-scaling exponent γ defined in Eq. (2) for the state points studied (Fig. 1). Closed symbols are isomorph state-point data and half open circles are isochore and isotherm data. Data are given for (a)–(c) state points with γ below 50 and (d)–(f) all state points: (a) γ as a function of the density, (b) γ as a function of the pressure, (c) γ as a function of the temperature, (d) γ as a function of the density in a log-log plot, (e) γ as a function of the pressure in a log-log plot, and (f) γ as a function of the temperature in a log-log plot. γ is clearly primarily a function of the temperature. The dashed line in (f) marks the low-temperature limit of the mean-field theory [Eq. (19)].

our primary focus, the arguments given below apply to any truncated purely repulsive potential.

In general, the partition function of the configurational degrees of freedom is given by $Z \propto \int_{V^N} d\mathbf{r}_1 \cdots d\mathbf{r}_N \exp[-\sum_{i<j} v(r_{ij})/k_B T]$. At low densities it is reasonable to regard the pair distances as uncorrelated, i.e., to treat the interactions in a mean-field way. This leads to the approximation $Z \propto Z_s^N$, in which $Z_s = \int_V d\mathbf{r} \exp[-v_s(\mathbf{r})/k_B T]$ is the partition function of a single particle moving in the potential $v_s(\mathbf{r})$ of all other particles frozen in space. In the low-density limit, none of the frozen particles overlap and Z_s has two contributions, one for the positions for which $v(\mathbf{r}) = 0$ and one for the positions at which the particle interacts with one of the frozen particles. The former is the free volume that in the low-density limit approaches the entire volume V. The latter is N times the following integral (putting, for simplicity, $k_B = 1$ in this section):

$$Z_1(T) = \int_0^{r_c} 4\pi r^2 \exp\left(-\frac{v(r)}{T}\right) dr. \qquad (8)$$

In terms of $Z_1(T)$ the single-particle partition function is thus in the thermodynamic limit given by

$$\frac{Z_s(\rho, T)}{N} = Z_1(T) + \frac{1}{\rho}. \qquad (9)$$

Based on the above, any pair-defined quantity $A(r)$ that is zero for $r > r_c$ has an expectation value that is computed as (in which $p(r) = 4\pi r^2 \exp[-v(r)/T]$ is the unnormalized

probability)

$$\langle A \rangle = \int_0^{r_c} \frac{A(r) p(r) dr}{Z_s(\rho, T)}. \qquad (10)$$

Based on Eqs. (2) and (1), one gets

$$\gamma(\rho, T) = \frac{\langle wv \rangle - \langle w \rangle \langle v \rangle}{\langle v^2 \rangle - \langle v \rangle^2} \qquad (11)$$

and

$$R(\rho, T) = \frac{\langle wv \rangle - \langle w \rangle \langle v \rangle}{\sqrt{(\langle w^2 \rangle - \langle w \rangle^2)(\langle v^2 \rangle - \langle v \rangle^2)}}. \qquad (12)$$

Figure 4 compares the predictions of the mean-field theory (lines) to data along isomorphs and isochores. There is good overall agreement. Systematic deviations are visible in Figs. 4(b) and 4(d), however, which focus on densities that are not low enough to avoid frozen-particle overlap.

We proceed to discuss the low-density limit in which $Z_s \to \infty$. Terms that involve a single expectation value ($\langle v^2 \rangle$, $\langle w^2 \rangle$, and $\langle wu \rangle$) scale as $1/Z_s$, while terms that involve a multiplication of expectation values, i.e., $\langle v \rangle^2$, $\langle w \rangle^2$, and $\langle v \rangle \langle w \rangle$, scale as $1/Z_s^2$. Consequently, at low densities one can neglect terms that involve multiplications of expectation values [18,33,60,61], leading to

$$\gamma(T) = \langle wv \rangle / \langle v^2 \rangle \qquad (13)$$

and

$$R(T) = \langle wv \rangle / \sqrt{\langle w^2 \rangle \langle v^2 \rangle}. \qquad (14)$$
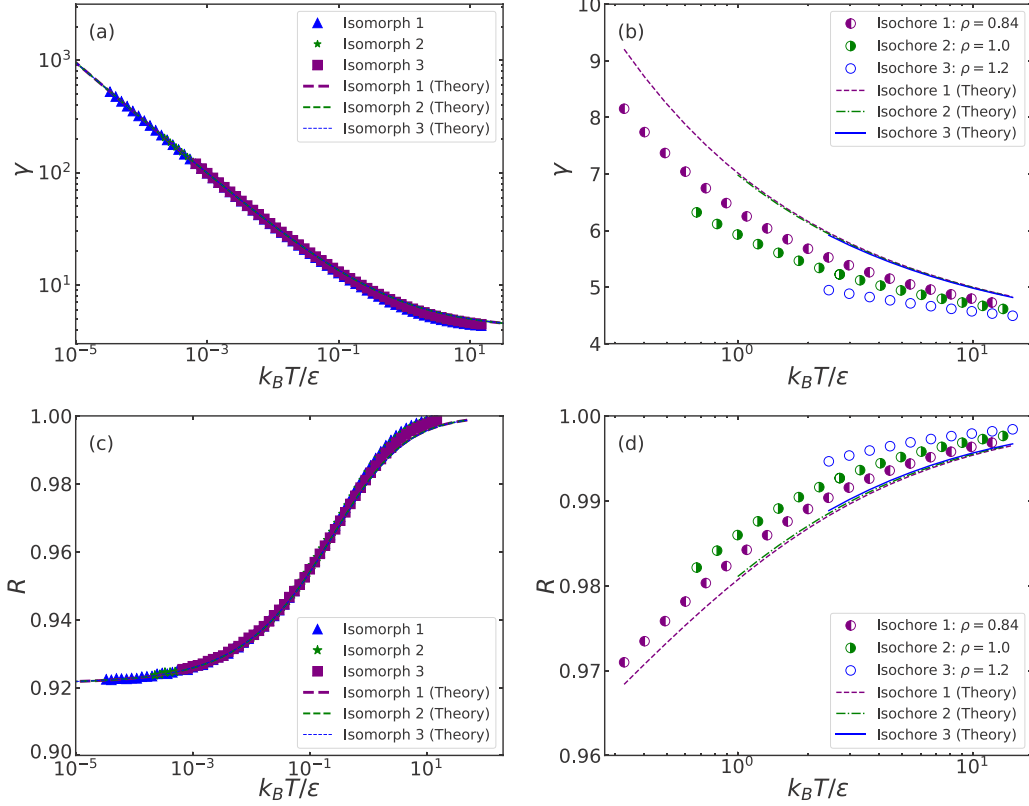
FIG. 4. Comparison of the predictions of the mean-field theory for γ and R as functions of the temperature (lines) to simulation results. (a) and (c) Results along the three isomorphs. (b) and (d) Results along the three isochores, focusing on higher densities where the mean-field theory is not expected to be accurate.

Note that these averages do not depend on Z_s since both numerators and denominators scale as $1/Z_s$. This implies that γ and R at low densities depend only of T, which explains the observation in Fig. 3.

Consider now the further assumption of a low temperature. In that case the probability distribution $p(r)$ concentrates near r_c and one can expand around $x \equiv r_c - r = 0$ by writing the pair potential as

$$v(x) = k_1 x + \frac{k_2 x^2}{2} + \frac{k_3 x^3}{6} + \cdots . \tag{15}$$

The pair virial then becomes [15]

$$w(x) = (r_c - x)\left(\frac{k_1}{3} + \frac{k_2 x}{3}\right) + \frac{k_3 r_c x^2}{6} + O(x^3). \tag{16}$$

For the WCA potential $k_1 = 0$ and $k_2 = 36\sqrt[3]{4}$. Since $p(x)$ is concentrated near $x = 0$, the upper limit of the integral (17) may be extended to infinity, leading to

$$\langle A \rangle = \int_0^\infty \frac{A(x)p(x)dx}{Z} \quad (T \to 0), \tag{17}$$

in which

$$p(x) = 4\pi (r_c - x)^2 \exp\left(-\frac{k_2 x^2}{2T}\right). \tag{18}$$

The Gaussian integrals can be evaluated by hand or, e.g., using the SYMPY PYTHON library for symbolic mathematics. We find

that γ and R are given by

$$\gamma_0 = \frac{4r_c\sqrt{2k_2}}{9\sqrt{\pi T}} = \frac{16}{3\sqrt{\pi T}} \quad (T \to 0) \tag{19}$$

and

$$R_0 = \sqrt{\frac{8}{3\pi}} = 0.921\ldots \quad (T \to 0). \tag{20}$$

Figure 5 shows the mean-field predictions for γ and R at $T = 0.01$ plotted as a function of the density. As expected, the theory works well at low densities, even though one is here still not quite at the $T \to 0$ limit marked by the horizontal lines.

V. VARIATION OF STRUCTURE AND DYNAMICS ALONG ISOTHERMS, ISOCHORES, AND ISOMORPHS

The considerable γ variation of the WCA system means that it cannot be described approximately by an Euler-homogeneous potential-energy function. This section investigates to which degree the reduced-unit structure and dynamics are, nevertheless, invariant along isomorphs 1–3. Isomorph invariance is rarely exact, so in order to put the simulation results into perspective, we present also results for the variation of the reduced-unit structure and dynamics along isotherms and isochores. As a measure of the structure, we look at the radial distribution function (RDF) as a function of the radial distance. As a measure of the dynamics, we look at the mean-square displacement (MSD) as a function
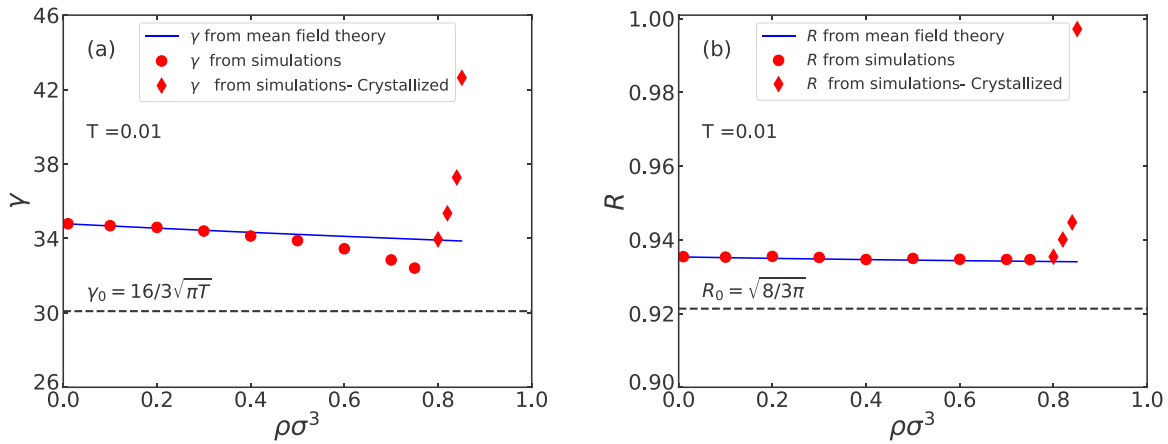
FIG. 5. Density dependence of (a) γ and (b) R at $T = 0.01$. The full blue lines are the mean-field theory predictions. The horizontal black dashed lines mark the low-temperature limits of the mean-field theory. Results are also shown for high-density samples that crystallized during the simulations.
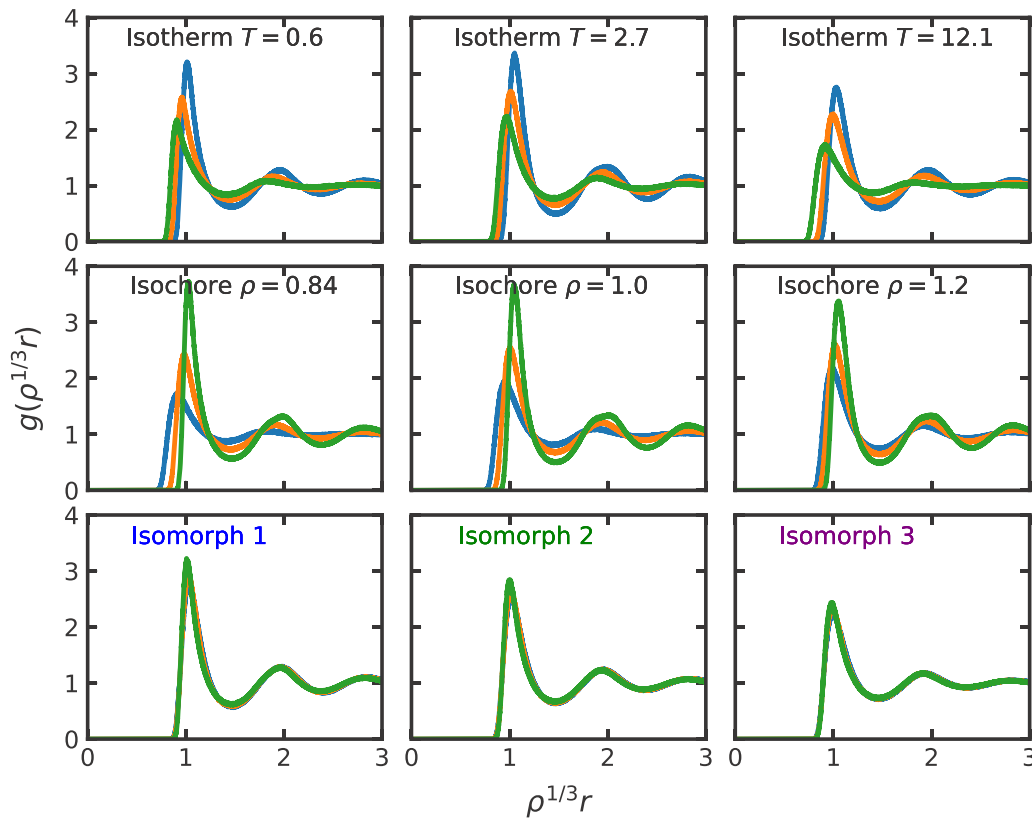

FIG. 6. Reduced-unit radial distribution functions for the three isotherms, isochores, and isomorphs (Fig. 1). The green curves give the lowest temperature and density, the orange curves give the intermediate temperature and density, and the blue curves give the highest temperature and density. Although the first-peak maximum is not entirely isomorph invariant, in comparison to isotherms and isochores we see an excellent RDF invariance along the isomorphs. This is the case even though the density variation of the isotherms and the temperature variation of the isochores are somewhat smaller than those of the isomorphs (compare Fig. 1). For the isotherms, the green curves give data for $(\rho, T) = (0.56, 0.60)$, $(0.82, 2.72)$, and $(0.81, 12.1)$; the orange curves for $(\rho, T) = (0.69, 0.60)$, $(1.0, 2.72)$, and $(1.21, 12.1)$; and the blue curves for $(\rho, T) = (0.84, 0.60)$, $(1.22, 2.72)$, and $(1.47, 12.1)$. For the isochores, the green curves give data for $(\rho, T) = (0.84, 0.33)$, $(1.00, 0.82)$, and $(1.21, 2.44)$; the orange curves for $(\rho, T) = (0.84, 1.99)$, $(1.00, 3.32)$, and $(1.21, 6.64)$; and the blue curves for $(\rho, T) = (0.84, 14.72)$, $(1.00, 13.46)$, and $(1.21, 14.78)$. For the isomorphs, the green curves give data for the reference state points $(\rho, T) = (0.84, 0.60)$, $(0.84, 1.00)$, and $(0.84, 2.00)$; the orange curves for $(\rho, T) = (1.06, 2.43)$, $(1.04, 3.32)$, and $(0.94, 3.64)$; and the blue curves for $(\rho, T) = (1.57, 14.72)$, $(1.40, 13.46)$, and $(1.26, 14.78)$.
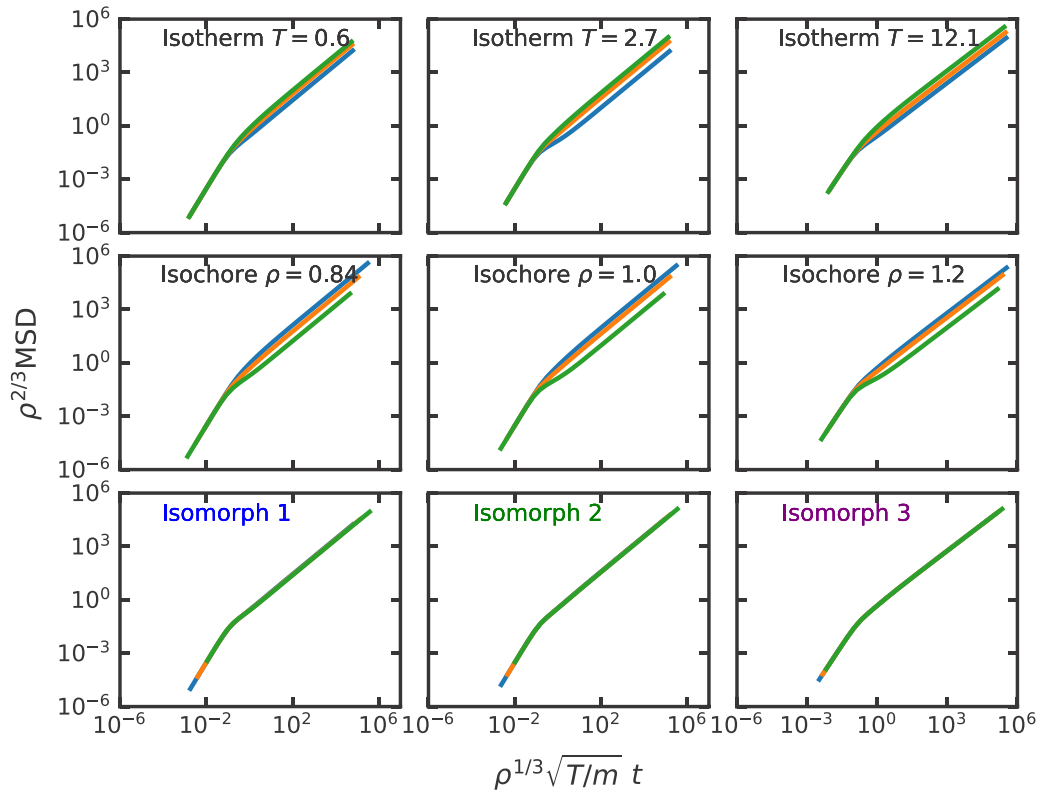
FIG. 7. Reduced-unit radial mean-square displacement plotted against time for the three isotherms, isochores, and isomorphs (Fig. 1). The state points and color codings are the same as in Fig. 6. The dynamics is isomorph invariant to a very good approximation.

of the time, as well as of the reduced diffusion coefficient $\tilde{D}$ identified from the long-time MSD.

Starting with structure, Fig. 6 shows reduced-unit RDF data along the three isotherms, isochores, and isomorphs of Fig. 1. The isotherms span almost the same density range and the isochores span almost the same temperature range as the corresponding isomorphs (restricted to the equilibrium liquid phase, i.e., to data above the freezing line). Along the isomorphs the RDFs show some variation at the first peak maximum (bottom row), but in comparison to the isotherms and isochores, there is excellent overall isomorph invariance of the RDF.

For all three isomorphs we find that the peak height increases as the temperature decreases. This is an effect of larger γ resulting in a higher first peak, which may be understood as follows. Consider the IPL pair-potential system with $v(r) \propto r^{-n}$, which has $\gamma = n/3$ and perfect isomorphs [62]. The larger n is, the more harshly repulsive the forces are. From the Boltzmann probability of finding two particles at the distance r, proportional to $\exp[-v(r)/k_B T]$, it follows that particle near encounters become less likely as $n \to \infty$, thus suppressing the RDF at distances below the first peak. If there is isomorph invariance of the number of particles within the first coordination shell, as n increases some of the RDF must therefore move from small r to larger r within the first coordination shell, resulting in a higher first peak. This argument has recently been confirmed by the observation that the bridge function, a fundamental quantity of liquid-state theory [54], is isomorph invariant to a very good approxima-

tion [63]. A similar increase of the height of the first RDF peak with increasing γ has been observed for the exponential system (Fig. 5 in Ref. [33]). In that case it was a much less dramatic effect, however, because the exponential system's γ variation at the investigated state points covered less than a factor of 3 compared to more than a factor of 100 for the WCA state points studied here. Interestingly, for both systems the data imply that $\gamma \to \infty$ as $T \to 0$ along an isomorph, i.e., both systems become more and more hard-sphere-like as the temperature is lowered.

Proceeding to investigate the dynamics, Fig. 7 shows data for the reduced-unit MSD as a function of the reduced time along the three isotherms, isochores, and isomorphs. There is only invariance along the isomorphs. Along the isotherms, the lowest density (green) gives rise to the largest reduced diffusion coefficient. This is because the mean collision length increases when the density is decreased. Along the isochores, the lowest temperature (green) has the smallest reduced diffusion coefficient. This is because the effective hard-sphere radius increases when temperature is decreased, leading to a smaller mean-collision length. In MD units, the MSDs are also not invariant along the isotherms or isochores (data not shown); thus the lack of invariance for the isotherms and isochores is not a consequence of the use of reduced units. In regard to the isomorph data, with Fig. 6 in mind we conclude that the noninvariant first-peak heights of the RDFs along the isomorphs have little influence on the dynamics. This is consistent with expectations from liquid-state quasiuniversality, according to which many systems have structure and
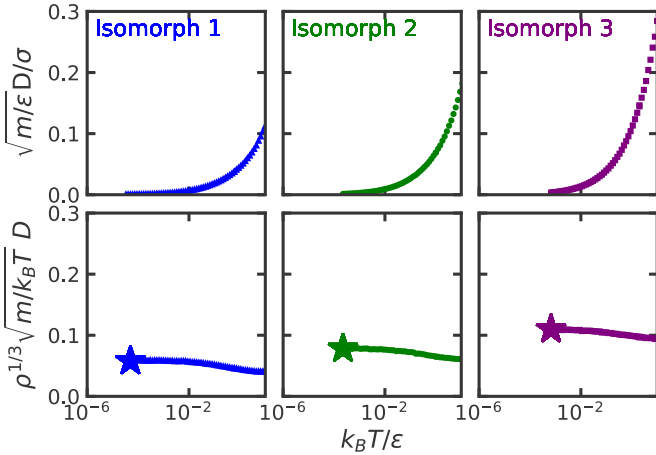
FIG. 8. Diffusion coefficients along isomorphs 1–3 in MD units (top row) and in reduced units (bottom row), plotted as functions of the logarithm of the temperature. When given in MD units, the diffusion coefficients vary significantly along the isomorphs, while they are fairly constant in reduced units. This illustrates the importance of using reduced units when checking for isomorph invariance. From end point to end point of the isomorphs, the variation in the reduced diffusion coefficient $\tilde{D}$ is, respectively, 39%, 23%, and 14%. The corresponding numbers are 1000%, 880%, and 549% along the isochores and 214%, 893%, and 305% along the isotherms.
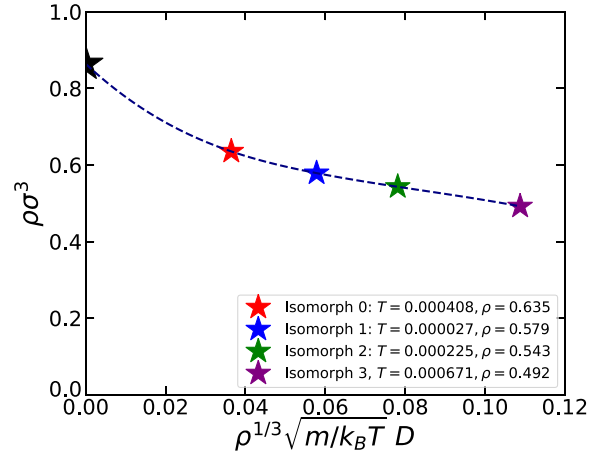

FIG. 9. Reduced diffusion coefficients at the lowest temperature and density for isomorphs 1–3 supplemented by data for isomorph 0, plotted versus the density of the lowest-temperature state point simulated on the isomorph in question. The points are fitted by a cubic spline function (dashed curve), which by construction goes through the random close packing (rcp) density ($\rho = 0.864$) marked by the half black star on the y axis. As rcp is approached, one expects $\tilde{D} \to 0$ because the system jams. This is consistent with our data. The rcp density is calculated as follows. With $r_c = 2^{1/6}$ one finds $V_{\text{sphere}} = \pi r_c^3 / 6 = 0.740$. The rcp volume fraction is roughly 64%; setting this equal to ρV_{sphere}, one arrives at $\rho = 0.864$.

dynamics similar to those of the exponential generic liquid system, which as mentioned also exhibits varying first-peak heights along its isomorphs [33].

The reduced diffusion coefficient $\tilde{D} \equiv \rho^{1/3} \sqrt{m/k_B T} \, D$ is extracted from the data in Fig. 7 by making use of the fact that the long-time reduced MSD is $6\tilde{D}\tilde{t}$. Figure 8 shows how both D and $\tilde{D}$ vary along the three isomorphs. The top row demonstrates a large variation in D along each isomorph. The bottom row shows $\tilde{D}$, which is rigorously invariant for a system with perfect isomorphs ($R = 1$). This is not the case for the WCA system, but the variation is below 40% for all three isomorphs in situations where the temperature varies by more than four orders of magnitude. Thus the reduced diffusion coefficient is isomorph invariant to a good approximation.

Figure 8 suggests that $\tilde{D}$ stabilizes as $T \to 0$, and for each isomorph one can tentatively identify this low-temperature limit. Figure 9 plots estimates of these limiting values obtained at the lowest density simulated on each isomorph. An obvious question is which density corresponds to $\tilde{D} = 0$. At very low temperature, because γ becomes very large the WCA system behaves increasingly as a system of hard spheres (HSs). The disordered HS system has a maximum density corresponding to the random closed-packed structure at roughly 64% packing fraction. In Fig. 9, the black star at $\tilde{D} = 0$ marks the corresponding density. Our data are consistent with a convergence to this point.

VI. DISCUSSION

We have studied three isomorphs of the WCA system and showed that along them the density-scaling exponent varies by more than a factor of 100. This extreme variation means that the WCA system cannot be considered as an effective

IPL system [15]. In the LJ case, the pair potential may be approximated by the so-called extended IPL pair potential, which is a sum of an IPL term $\sim r^{-18}$, a constant, and a term proportional to r [15]. The latter two terms contribute little to the fluctuations of virial and potential energy [15], which explains the strong correlations of the LJ system as well as why γ is close to 6 (not to 4 as one might guess from the repulsive r^{-12} term of the potential). The WCA situation is very different. Because the WCA system is purely repulsive, it has no liquid-gas phase transition and no liquid-gas coexistence region. This means that isomorphs may be studied over several orders of magnitude of temperature and, in particular, followed to very low temperatures. Interestingly, even here the strong-correlation property is maintained. At the same time, γ increases dramatically. Despite this, the reduced-unit structure and dynamics are both invariant to a good approximation along the isomorphs. The significant difference between the LJ and WCA systems in regard to isomorph properties is also emphasized by the fact that the density-scaling exponent γ of the LJ system is primarily a function of the density and well described by Eq. (3). This is explained by the above-mentioned approximate extended IPL pair-potential argument [15].

The finding that R and γ of the WCA system are both primarily functions of the temperature is accounted for by a mean-field theory based on the assumption of statistically independent pair interactions. The same feature is observed for the exponential pair-potential system [33], and also here both R and γ at low densities primarily depend on the temperature. Another situation where this is expected to apply is for the repulsive Yukawa pair-potential system at low densities [29,30].

In summary, the WCA systems presents a striking case where the density-scaling exponent is very far from being constant throughout the thermodynamic phase diagram [35,36]. Nevertheless, the system is *R*-simple and has good isomorph invariance of the structure and dynamics.

APPENDIX: USING THE RUNGE-KUTTA METHOD FOR TRACING OUT ISOMORPHS EFFICIENTLY

The density-scaling exponent γ is the slope of the lines of constant S_{ex} in the $(\ln T, \ln \rho)$ plane [Eq. (2)]. By numerical integration one can, from Eq. (2), compute the lines of constant S_{ex}, the configurational adiabats, which are isomorphs for any *R*-simple system. The density-scaling exponents required for the integration are determined from the thermal equilibrium virial potential-energy fluctuations in an NVT simulation [Eq. (2)]. In the following we denote the theoretical slope by f, i.e., the slope without the unavoidable statistical noise of any MD simulation. Let (x, y) be $(\ln \rho, \ln T)$ [occasionally it is better to choose instead $(x, y) = (\ln T, \ln \rho)$]. In this notation, let

$$\frac{dy}{dx} = f(x, y) \tag{A1}$$

be the first-order differential equation to be integrated. Several methods have been developed to do this numerically [64]. The simplest one is Euler's method. Imagine that one has estimated the slope at some point (x_i, y_i) by computing $\gamma = f(x_i, y_i)$ from the virial potential-energy fluctuations by means of Eq. (2). The point (x_{i+1}, y_{i+1}) is then calculated from

$$x_{i+1} = x_i + h,$$
$$y_{i+1} = y_i + hf(x_i, y_i) + O(h^2). \tag{A2}$$

Here h is the size of the numerical integration step along x. The truncation error on the estimated y_{i+1} scales as h^2.

The statistical error on the numerical calculation of the slope f scales as $1/\sqrt{\tau}$, where τ is the simulation time. Thus, the statistical error on y_{i+1} scales as $h/\sqrt{\tau}$ (rounding errors from the finite machine precision are not relevant for the h's investigated here). The scaling of the total error is thus proportional to $h^2 + ch/\sqrt{\tau}$, in which c is a constant. We are interested, however, in the global truncation error, i.e., the accumulated error for some integration length Δx. Let $N = \Delta x/h$ be the number of steps needed to complete the integration. The total simulation time is $t = N(\tau + \tau_{\mathrm{eq}})$, where τ_{eq} is the time it takes for the system to come into equilibrium when temperature and density are changed. Thus $\tau = t/N - \tau_{\mathrm{eq}}$, and with $h = \Delta x/N$ the statistical error on y is $ch/\sqrt{\tau} = c\Delta x/\sqrt{Nt - N^2\tau_{\mathrm{eq}}}$. The global error from truncation scales as N since it is systematic, while the statistical error scales as $\sqrt{N}$ due to its randomness. Thus, the total global error is proportional to $(\Delta x)^2/N + c\Delta x/\sqrt{t - N\tau_{\mathrm{eq}}}$. The first term is lowered by making N large, while the second term favors small N's and diverges as $N \to t/\tau_{\mathrm{eq}}$. Thus, since c is in general unknown, the optimal choice of N for a given t and Δx is not straightforward to determine. We give below a recipe for the optimal parameter choice. First, however, we show how to reduce the truncation error significantly by adopting a higher-order integration method, using the often favored fourth-order Runge-Kutta (RK4) method: For a given point (x_i, y_i), if one defines

$$k_1 = hf(x_i, y_i),$$
$$k_2 = hf\left(x_i + \frac{h}{2}, y_i + \frac{k_1}{2}\right),$$
$$k_3 = hf\left(x_i + \frac{h}{2}, y_i + \frac{k_2}{2}\right),$$
$$k_4 = hf(x_i + h, y_i + k_3), \tag{A3}$$

the next point (x_{i+1}, y_{i+1}) is computed as

$$x_{i+1} = x_i + h,$$
$$y_{i+1} = y_i + \frac{k_1}{6} + \frac{k_2}{3} + \frac{k_3}{3} + \frac{k_4}{6} + O(h^5). \tag{A4}$$
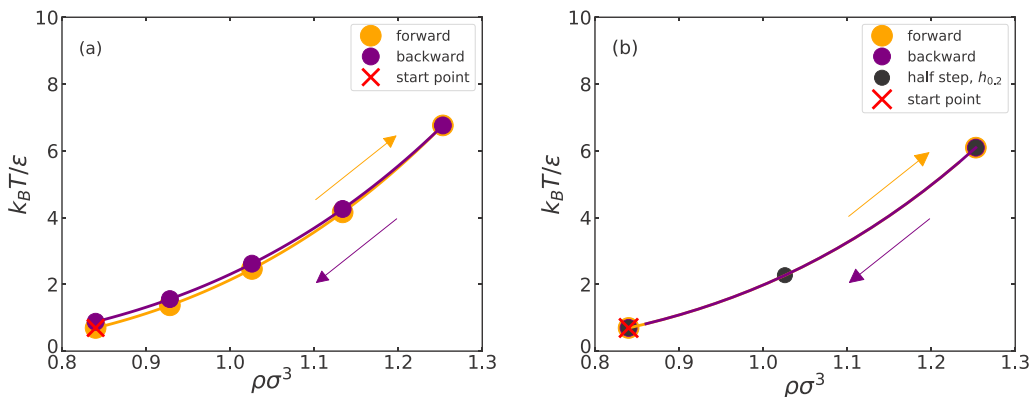

FIG. 10. Configurational adiabat of the WCA system traced out in the thermodynamic phase diagram for (a) the Euler method and (b) the RK4 method. The Euler integration uses a log-density step of size $h = 0.1$ (steps in density of $e^{0.1} - 1 \simeq 10\%$), while the RK4 uses $h = 0.4$, corresponding to a density variation of $e^{0.4} - 1 \simeq 50\%$. The temperature difference of the here presented combined forward-backward integration ΔT provides a convenient measure of the maximum error of the predicted temperature. We find $\Delta T \cong 0.186$ for the Euler algorithm and $\Delta T \cong 0.002$ for the RK4 algorithm. The solid lines are interpolations using a cubic Hermite spline.
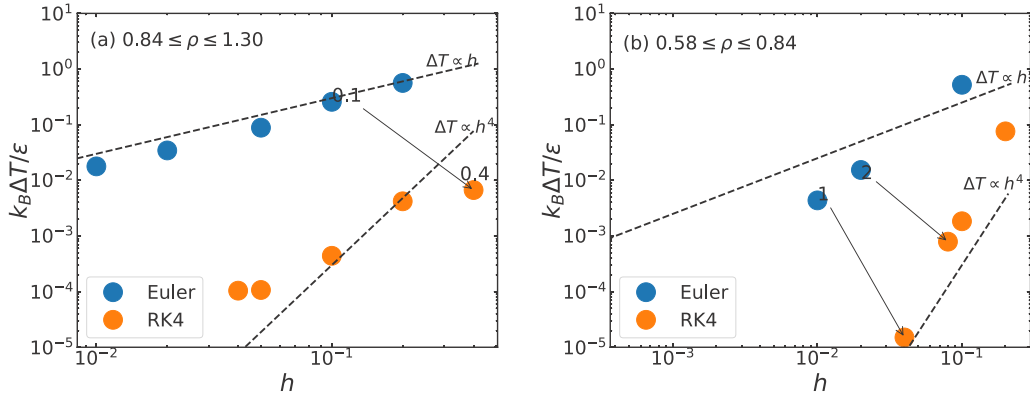
FIG. 11. (a) Temperature difference ΔT of the forward-backward integration in Fig. 10, for different steps sizes h. The blue circles show results for Euler integration and the orange circles show results for RK4 integration. The temperature difference measures the maximum error in the integration interval $0.84 \leqslant \rho \leqslant 1.30$. The RK4 is significantly more accurate than the Euler algorithm, which allows for larger h steps. The dashed lines indicate the expected scaling of the global error from truncation; deviations stem from statistical errors on the estimated slopes (slopes are evaluated using simulations lengths of $\tau = 655$). The arrow connects Euler and RK4 calculations with approximately the same computational cost (see Fig. 10). (b) Same analysis for the integration interval $0.58 \leqslant \rho \leqslant 0.84$.

While the simple Euler method has a truncation error scaling as $O(h^2)$, the truncation error of RK4 scales as $O(h^5)$. This allows for significantly larger steps along x and thus smaller N. From the same type of arguments as given above for the Euler method, the global error of the RK4 method scales approximately as $(\Delta x)^5/N^4 + c\Delta x/\sqrt{t - N\tau_{\text{eq}}}$, where c is a (new) unknown constant.

To compare the Euler and RK4 methods, we use each of them for integrating from the initial state point $(\rho, T) = (0.84, 0.694)$ to density 1.25 and back again to the initial density of 0.84 (see Fig. 10). This involves a γ variation from 6.825 at the initial density to 4.539 at $\rho = 1.25$. The difference between the final temperature of the down integration and the initial temperature, denoted by ΔT, provides a measure of the maximum temperature error. Ideally $\Delta T = 0$. Since the RK4 involves four simulations per step, we compare its accuracy where h is four times larger than for the Euler method, which corresponds to approximately the same wall-clock time for the computation. With this constraint, the RK4 is still about two orders of magnitude more accurate: We find $\Delta T = 0.186$ for the Euler algorithm and $\Delta T \cong 0.002$ for RK4. Figure 11 shows estimates of the maximum error ΔT for several values of h. To focus on the truncation error, we performed long-time simulations with $\tau \cong 650$. Nonetheless, this analysis demonstrates that a significantly smaller N (larger h) is allowed for with the RK4.

Since the RK4 algorithm allows for large h, it can be necessary to interpolate in order to identify additional state points on the isomorph. The solid lines in Fig. 10 show such interpolations using a cubic Hermite spline. Define x_ϕ as a point between the two adjacent points x_i and x_{i+1}, i.e., let $x_i \leqslant x_\phi < x_{i+1}$, where $x_\phi = x_i + \phi[x_{i+1} - x_i]$ and $0 \leqslant \phi \leqslant 1$. The interpolated y_ϕ is given by the third-degree polynomial $y_\phi = Ax_\phi^3 + Bx_\phi^2 + Cx_\phi + D$, where $y_\phi = y_i + [y_{i+1} - y_i][a\phi^3 + b\phi^2 + c\phi]$. For simplicity, we introduce the notation $y'_\phi = [y_\phi - y_i]/[y_{i+1} - y_i]$ and write the polynomial as $y'_\phi = a\phi^3 + b\phi^2 + c\phi$. The coefficients yielding smooth first derivative are $a = f'_i + f'_{i+1} - 2$, $b = 3 - 2f'_i - f'_{i+1}$,

and $c = f'_i$, in which $f'_i = f_i(x_{i+1} - x_i)/(y_{i+1} - y_i)$ and $f'_{i+1} = f_{i+1}(x_{i+1} - x_i)/(y_{i+1} - y_i)$ are reduced slopes at the start and end points, respectively. The f' slopes are given by known γ's along the configurational adiabat; thus no extra simulations are needed to evaluate the interpolation.

We investigated the local error by comparing a full h step to two half steps of size $h/2$. The small black circle near the middle of Fig. 10(b) shows the results of two such half steps. The truncation error for the half-step approach is then raised to the sixth order [64], one order higher than RK4 (the consequence is that one must perform twice as many simulations for each integration step). The triangles in Fig. 12 show the resulting T_{i+1} starting from the reference state point $(\rho, T) = (0.84, 0.694)$, using a full step with $h = 0.4$ and
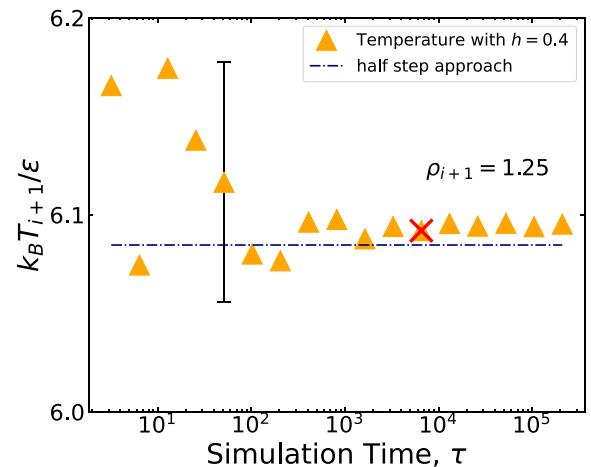

FIG. 12. Difference in temperature between using a full step of $h = 0.4$ and two half steps of $h = 0.2$ when integrating from $\rho = 0.84$ up to $\rho = 1.25$, plotted against the simulation time per slope evaluation. The desired h can change and the simulation time changes accordingly. The error bar indicates the bad statistics with few blocks mentioned in the text, computed from Eq. (28) in Ref. [65]. The red $\times$ marks the simulation time used in the paper.
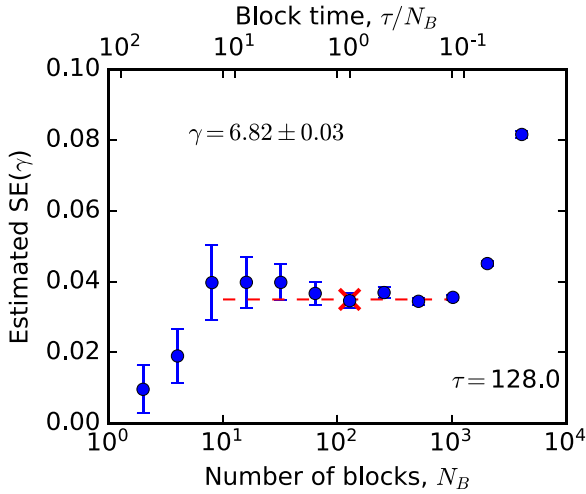
FIG. 13. Estimate of the statistical error on γ from the blocking method. The analysis indicates that $N_B = 128$ is a good choice for the number of blocks. This gives $\mathrm{SE}(\gamma) = 0.03$ on the estimated $\gamma = 6.82$.
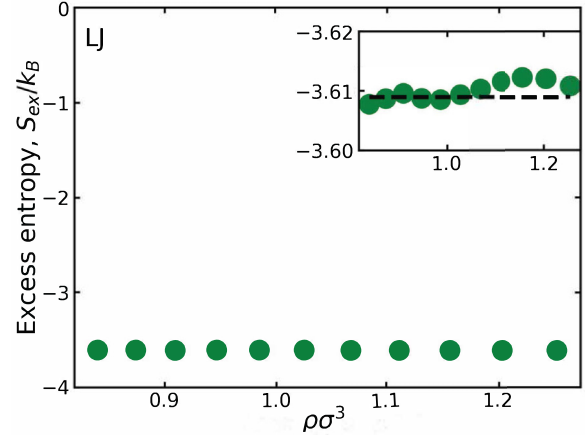

FIG. 14. Excess entropy values plotted against the densities of the state points on the configurational adiabat traced out for the single-component LJ system starting from the triple point ($\rho = 0.84, T = 0.694$) using RK4 with $h = 0.04$. The view is zoomed in on the values to see the deviation from the average value, the black dotted line.

varying τ's. For comparison, the dashed line results from long-time simulations using the half-step algorithm. The distance from triangles to the dashed line provides an estimate of the total error. For short simulation times (small τ's) the statistical error dominates, as shown by the scatter. The truncation error dominates at long simulation times, as shown by the triangles' systematic deviation from the dashed line. For efficient calculation we suggest choosing h and τ such that the statistical and truncation errors are of the same order of magnitude. The red cross in Fig. 12 indicates the simulation time τ used for the figures in the paper.

The above analysis to arrive at the optimal computation time τ is tedious and involves computationally expensive simulations. We proceed to suggest an efficient optimization recipe that utilizes the fact that the local statistical error of the slopes can be estimated by dividing a given simulation into blocks. If the simulation time for each block is sufficiently long, the blocks are statistically independent. The 67% confidence standard error is then given by $\mathrm{SE}(\gamma) = \sqrt{\mathrm{Var}(\gamma)/(N_B - 1)}$, where $\mathrm{Var}(\gamma)$ is the variance of the γ's using N_B blocks [65]. If the blocks are independent, $\mathrm{Var}(\gamma)$ scales as N_B and $\mathrm{SE}(\gamma)$ will be independent of the number of blocks. If we divide the simulation into few blocks, $\mathrm{Var}(\gamma)$ may give a bad estimate of the underlying distribution's theoretical variance. On the other hand, if one divides the simulation into many blocks, the simulation time for each block (τ/N_B) may be brief and the blocks are not independent. In effect, the above formula for $\mathrm{SE}(\gamma)$ gives an overestimate. The optimal N_B is determined by tests of several different N_B, as shown in Fig. 13 (the red cross corresponds to a good choice of $N_B = 128$). The statistical error on y_{i+1} can now be estimated as $\mathrm{SE}(y_{i+1}) = \mathrm{SE}(\gamma)h/2$. Here $2 = \sqrt{4}$ enters since the RK4 algorithm includes four independent estimates

of slopes (the factor is unity for the Euler algorithm and $\sqrt{8}$ for the double-step RK4).

Based on the above analysis, we propose the following recipe for efficient and accurate computation of a configurational adiabat.

(i) Make an NVT simulation at a reference state point of temperature T_0 and density ρ_0. The simulation time τ should be sufficiently long that the equilibration time τ_{eq} can be determined using any standard method (e.g., as the time when the mean-square displacement has reached the diffusive limit). Use the block method to determine $\mathrm{SE}(\gamma)$, using only the equilibrated part of the trajectory.

(ii) Choose h. Make a full RK4 step and estimate the local statistical error using $\mathrm{SE}(y_{i+1}) = h\,\mathrm{SE}(\gamma)/\sqrt{4}$. Use the RK4 two–half-step approach to estimate the total local error. If the total local error is unacceptably large, then either (a) increase τ if the statistical error is of the same magnitude as the total error or (b) decrease h if the total error is larger than the statistical error. Small errors suggest that the simulation time τ could be decreased or that h can be increased to make the calculation more efficient; h may safely be increased or τ decreased if the statistical and total errors are of similar magnitude.

(iii) Compute adiabatic state points using the RK4 algorithm with the parameters determined in the above steps. Based on these, a continuous curve can be produced by interpolation using a cubic spline.

(iv) Estimate the maximum error by integrating backward. This error estimate quantifies the accuracy of the computed adiabat.

As a consistency check of this recipe, Fig. 14 shows the excess entropy from the equation of state (EOS) of the single-component LJ system in Ref. [66]. The agreement with the configurational adiabat of this EOS is excellent.

[1] C. Alba-Simionesco, A. Cailliaux, A. Alegria, and G. Tarjus, Scaling out the density dependence of the alpha relaxation in glass-forming polymers, Europhys. Lett. **68**, 58 (2004).

[2] C. M. Roland, S. Hensel-Bielowka, M. Paluch, and R. Casalini, Supercooled dynamics of glass-forming liquids and polymers under hydrostatic pressure, Rep. Prog. Phys. **68**, 1405 (2005).

[3] E. R. Lopez, A. S Pensado, J. Fernandez, and K. R. Harris, On the density scaling of pVT data and transport properties for molecular and ionic liquids, J. Chem. Phys. **136**, 214502 (2012).

[4] K. Adrjanowicz, M. Paluch, and J. Pionteck, Isochronal superposition and density scaling of the intermolecular dynamics in glass-forming liquids with varying hydrogen bonding propensity, RSC Adv. **6**, 49370 (2016).

[5] D. Gundermann, U. R. Pedersen, T. Hecksher, N. P. Bailey, B. Jakobsen, T. Christensen, N. B. Olsen, T. B. Schrøder, D. Fragiadakis, R. Casalini, C. M. Roland, J. C. Dyre, and K. Niss, Predicting the density-scaling exponent of a glass-forming liquid from Prigogine-Defay ratio measurements, Nat. Phys. **7**, 816 (2011).

[6] D. Kivelson, G. Tarjus, X. Zhao, and S. A. Kivelson, Fitting of viscosity: Distinguishing the temperature dependences predicted by various models of supercooled liquids, Phys. Rev. E **53**, 751 (1996).

[7] N. Gnan, T. B. Schrøder, U. R. Pedersen, N. P. Bailey, and J. C. Dyre, Pressure-energy correlations in liquids. IV. "Isomorphs" in liquid phase diagrams, J. Chem. Phys. **131**, 234504 (2009).

[8] J. C. Dyre, Hidden scale invariance in condensed matter, J. Phys. Chem. B **118**, 10007 (2014).

[9] Y. Rosenfeld, Relation between the transport coefficients and the internal entropy of simple systems, Phys. Rev. A **15**, 2545 (1977).

[10] J. C. Dyre, Perspective: Excess-entropy scaling, J. Chem. Phys. **149**, 210901 (2018).

[11] T. B. Schrøder and J. C. Dyre, Simplicity of condensed matter at its core: Generic definition of a Roskilde-simple system, J. Chem. Phys. **141**, 204502 (2014).

[12] U. R. Pedersen, N. P. Bailey, T. B. Schrøder, and J. C. Dyre, Strong Pressure-Energy Correlations in van der Waals Liquids, Phys. Rev. Lett. **100**, 015701 (2008).

[13] N. P. Bailey, U. R. Pedersen, N. Gnan, T. B. Schrøder, and J. C. Dyre, Pressure-energy correlations in liquids. I. Results from computer simulations, J. Chem. Phys. **129**, 184507 (2008).

[14] D. M. Heyes and A. C. Branka, Physical properties of soft repulsive particle fluids, Phys. Chem. Chem. Phys. **9**, 5570 (2007).

[15] N. P. Bailey, U. R. Pedersen, N. Gnan, T. B. Schrøder, and J. C. Dyre, Pressure-energy correlations in liquids. II. Analysis and consequences, J. Chem. Phys. **129**, 184508 (2008).

[16] T. B. Schrøder, N. Gnan, U. R. Pedersen, N. P. Bailey, and J. C. Dyre, Pressure-energy correlations in liquids. V. Isomorphs in generalized Lennard-Jones systems, J. Chem. Phys. **134**, 164505 (2011).

[17] T.-J. Yoon, M. Y. Ha, E. A. Lazar, W. B. Lee, and Y.-W. Lee, Topological extension of the isomorph theory based on the Shannon entropy, Phys. Rev. E **100**, 012118 (2019).

[18] A. K. Bacher, T. B. Schrøder, and J. C. Dyre, The EXP pair-potential system. I. Fluid phase isotherms, isochores, and quasiuniversality, J. Chem. Phys. **149**, 114501 (2019).

[19] A. K. Bacher, U. R. Pedersen, T. B. Schrøder, and J. C. Dyre, The EXP pair-potential system. IV. Isotherms, isochores, and isomorphs in the two crystalline phases, J. Chem. Phys. **152**, 094505 (2020).

[20] T. S. Ingebrigtsen, T. B. Schrøder, and J. C. Dyre, Isomorphs in model molecular liquids, J. Phys. Chem. B **116**, 1018 (2012).

[21] D. Fragiadakis and C. M. Roland, Intermolecular distance and density scaling of dynamics in molecular liquids, J. Chem. Phys. **150**, 204501 (2019).

[22] K. Koperwas, A. Grzybowski, and M. Paluch, Virial–potential-energy correlation and its relation to density scaling for quasireal model systems, Phys. Rev. E **102**, 062140 (2020).

[23] T. S. Ingebrigtsen and H. Tanaka, Effect of size polydispersity on the nature of Lennard-Jones liquids, J. Phys. Chem. B **119**, 11052 (2015).

[24] D. E. Albrechtsen, A. E. Olsen, U. R. Pedersen, T. B. Schrøder, and J. C. Dyre, Isomorph invariance of the structure and dynamics of classical crystals, Phys. Rev. B **90**, 094106 (2014).

[25] T. S. Ingebrigtsen, J. R. Errington, T. M. Truskett, and J. C. Dyre, Predicting how Nanoconfinement Changes the Relaxation Time of a Supercooled Liquid, Phys. Rev. Lett. **111**, 235901 (2013).

[26] A. A. Veldhorst, J. C. Dyre, and T. B. Schrøder, Scaling of the dynamics of flexible Lennard-Jones chains, J. Chem. Phys. **141**, 054904 (2014).

[27] F. Hummel, G. Kresse, J. C. Dyre, and U. R. Pedersen, Hidden scale invariance of metals, Phys. Rev. B **92**, 174116 (2015).

[28] L. Friedeheim, J. C. Dyre, and N. P. Bailey, Hidden scale invariance at high pressures in gold and five other face-centered-cubic metal crystals, Phys. Rev. E **99**, 022142 (2019).

[29] A. A. Veldhorst, T. B Schrøder, and J. C. Dyre, Invariants in the Yukawa system's thermodynamic phase diagram, Phys. Plasmas **22**, 073705 (2015).

[30] P. Tolias and F. L. Castello, Isomorph-based empirically modified hypernetted-chain approach for strongly coupled Yukawa one-component plasmas, Phys. Plasmas **26**, 043703 (2019).

[31] T. B. Schrøder, U. R. Pedersen, N. P. Bailey, S. Toxvaerd, and J. C. Dyre, Hidden scale invariance in molecular van der Waals liquids: A simulation study, Phys. Rev. E **80**, 041502 (2009).

[32] T. S. Ingebrigtsen, L. Bøhling, T. B. Schrøder, and J. C. Dyre, Thermodynamics of condensed matter with strong pressure-energy correlations, J. Chem. Phys. **136**, 061102 (2012).

[33] A. K. Bacher, T. B. Schrøder, and J. C. Dyre, The EXP pair-potential system. II. Fluid phase isomorphs, J. Chem. Phys. **149**, 114502 (2018).

[34] D. M. Heyes, D. Dini, L. Costigliola, and J. C. Dyre, Transport coefficients of the Lennard-Jones fluid close to the freezing line, J. Chem. Phys. **151**, 204502 (2019).

[35] A. Sanz, T. Hecksher, H. W. Hansen, J. C. Dyre, K. Niss, and U. R. Pedersen, Experimental Evidence for a State-Point-Dependent Density-Scaling Exponent of Liquid Dynamics, Phys. Rev. Lett. **122**, 055501 (2019).

[36] R. Casalini and T. C. Ransom, On the experimental determination of the repulsive component of the potential from high pressure measurements: What is special about twelve?" J. Chem. Phys. **151**, 194504 (2019).

[37] L. Bøhling, T. S. Ingebrigtsen, A. Grzybowski, M. Paluch, J. C. Dyre, and T. B. Schrøder, Scaling of viscous dynamics in simple liquids: Theory, simulation and experiment, New J. Phys. **14**, 113035 (2012).

[38] T. C. Ransom, R. Casalini, D. Fragiadakis, and C. M. Roland, The complex behavior of the "simplest" liquid: Breakdown of

density scaling in tetramethyl tetraphenyl trisiloxane, J. Chem. Phys. **151**, 174501 (2019).

[39] J. D. Weeks, D. Chandler, and H. C. Andersen, Role of repulsive forces in determining the equilibrium structure of simple liquids, J. Chem. Phys. **54**, 5237 (1971).

[40] D. Chandler, J. D. Weeks, and H. C. Andersen, Van der Waals picture of liquids, solids, and phase transformations, Science **220**, 787 (1983).

[41] A. de Kuijper, J. A. Schouten, and J. P. J. Michels, The melting line of the Weeks-Chandler-Anderson Lennard-Jones reference system, J. Chem. Phys. **93**, 3515 (1990).

[42] M. Bishop, A. Masters, and J. H. R. Clarke, Equation of state of hard and Weeks-Chandler-Andersen hyperspheres in four and five dimensions, J. Chem. Phys. **110**, 11449 (1999).

[43] D. Ben-Amotz and G. Stell, Reformulaton of Weeks-Chandler-Andersen perturbation theory directly in terms of a hard-sphere reference system, J. Phys. Chem. B **108**, 6877 (2004).

[44] A. E. Nasrabad, Thermodynamic and transport properties of the Weeks-Chandler-Andersen fluid: Theory and computer simulation, J. Chem. Phys. **129**, 244508 (2008).

[45] A. Ahmed and R. J. Sadus, Phase diagram of the Weeks-Chandler-Andersen potential from very low to high temperatures and pressures, Phys. Rev. E **80**, 061101 (2009).

[46] R. Benjamin and J. Horbach, Crystal growth kinetics in Lennard-Jones and Weeks-Chandler-Andersen systems along the solid-liquid coexistence line, J. Chem. Phys. **143**, 014702 (2015).

[47] B. Atreyee and D. J. Wales, Fragility and correlated dynamics in supercooled liquids, J. Chem. Phys. **153**, 124501 (2020).

[48] N. Dawass, P. Krüger, S. K. Schnell, O. A. Moultos, I. G. Economou, T. J. H. Vlugt, and J.-M. Simon, Kirkwood-Buff integrals using molecular simulation: Estimation of surface effects, Nanomaterials **10**, 771 (2020).

[49] F. Gußmann, S. Dietrich, and R. Roth, Toward a density-functional theory for the Jagla fluid, Phys. Rev. E **102**, 062112 (2020).

[50] A. Mirzaeinia and F. Feyzi, A perturbed-chain equation of state based on Wertheim TPT for the fully flexible LJ chains in the fluid and solid phases, J. Chem. Phys. **152**, 134502 (2020).

[51] T. P. O. Nogueira, H. O. Frota, F. Piazza, and J. R. Bordin, Tracer diffusion in crowded solutions of sticky polymers, Phys. Rev. E **102**, 032618 (2020).

[52] H. Tong and H. Tanaka, Role of Attractive Interactions in Structure Ordering and Dynamics of Glass-Forming Liquids, Phys. Rev. Lett. **124**, 225501 (2020).

[53] S. Ueda and K. Morita, Theoretical calculation of the free energy of mixing of liquid transition-metal alloys using a bond-order potential and thermodynamic perturbation theory, J. Non-Cryst. Solids **528**, 119743 (2020).

[54] J.-P. Hansen and I. R. McDonald, *Theory of Simple Liquids: With Applications to Soft Matter*, 4th ed. (Academic, New York, 2013).

[55] M. P. Allen and D. J. Tildesley, *Computer Simulation of Liquids* (Oxford Science, Oxford, 1987).

[56] N. P. Bailey, T. S. Ingebrigtsen, J. S. Hansen, A. A. Veldhorst, L. Bøhling, C. A. Lemarchand, A. E. Olsen, A. K. Bacher, L. Costigliola, U. R. Pedersen, H. Larsen, J. C. Dyre, and T. B. Schrøder, RUMD: A general purpose molecular dynamics package optimized to utilize GPU hardware down to a few thousand particles, SciPost Phys. **3**, 038 (2017).

[57] http://rumd.org, version 3.5 (Glass and Time, Roskilde, 2020).

[58] U. R. Pedersen, L. Costigliola, N. P. Bailey, T. B Schrøder, and J. C. Dyre, Thermodynamics of freezing and melting, Nat. Commun. **7**, 12386 (2016).

[59] R. Casalini and T. C. Ransom, On the pressure dependence of the thermodynamical scaling exponent γ, Soft Matter **16**, 4625 (2020).

[60] T. Maimbourg and J. Kurchan, Approximate scale invariance in particle systems: A large-dimensional justification, Europhys. Lett. **114**, 60002 (2016).

[61] T. Maimbourg, J. C. Dyre, and L. Costigliola, Density scaling of generalized Lennard-Jones fluids in different dimensions, SciPost Phys. **9**, 90 (2020).

[62] D. M. Heyes, D. Dini, and A. C. Branka, Scaling of Lennard-Jones liquid elastic moduli, viscoelasticity and other properties along fluid-solid coexistence, Phys. Status Solidi B **252**, 1514 (2015).

[63] F. L. Castello, P. Tolias, and J. C. Dyre, Testing the isomorph invariance of the bridge functions of Yukawa one-component plasmas, J. Chem. Phys. **154**, 034501 (2021).

[64] W. H. Press, S. A. Teukolsky, W. T. Vetterling, and B. P. Flannery, *Numerical Recipes: The Art of Scientific Computing*, 3rd ed. (Cambridge University Press, Cambridge, 2007).

[65] H. Flyvbjerg and H. G. Petersen, Error estimates on averages of correlated data, J. Chem. Phys. **91**, 461 (1989).

[66] J. Kolafa and I. Nezbeda, The Lennard-Jones fluid: An accurate analytic and theoretically-based equation of state, Fluid Phase Equilibr. **100**, 1 (1994).